THE JOURNAL OF PHYSICAL CHEMISTRY C

Article

Cite This: J. Phys. Chem. C 2017, 121, 26034-26043

pubs.acs.org/JPCC

Interlayer Coupling Behaviors of Boron Doped Multilayer Graphene

Guorui Wang,[†,§] Xiaoli Li,[‡] Yanlei Wang,[∥] Zhiyue Zheng,[†] Zhaohe Dai,[⊥] Xiaoying Qi,[†] Luqi Liu,[*,†] Zhihai Cheng,[†] Zhiping Xu,[∥] PingHeng Tan,[*,‡] and Zhong Zhang[*,†]

[†]CAS Key Laboratory of Nanosystem and Hierarchical Fabrication and CAS Center for Excellence in Nanoscience, National Center for Nanoscience and Technology, Beijing 100190, China

[‡]State Key Laboratory of Superlattices and Microstructures, Institute of Semiconductors, Chinese Academy of Sciences, Beijing 100083, P. R. China

[§]CAS Key Laboratory of Mechanical Behavior and Design of Materials, Department of Modern Mechanics, University of Science and Technology of China, Hefei 230026, China

[∥]Applied Mechanics Laboratory, Department of Engineering Mechanics and Center for Nano and Micro Mechanics, Tsinghua University, Beijing 100084, China

[⊥]Center for Mechanics of Solids, Structures and Materials, Department of Aerospace Engineering and Engineering Mechanics, The University of Texas at Austin, Austin, Texas 78712, United States

Supporting Information

ABSTRACT: It is fundamentally important to understand how the interlayer interaction of neighboring graphene sheets is influenced by chemical doping. Here we investigate the interlayer coupling of multilayer graphene doped with controlled boron content via the Raman-active in-plane shear mode. The experimental results reveal a remarkable decline in the interlayer shear modulus as boron content increases, which is a direct consequence of the enlarged interlayer spacing, further supported by the molecular dynamic (MD) simulations. Nanoindentation tests were conducted to clarify the influence of interlayer coupling behaviors on nanomechanical behaviors of boron-doped bilayer graphene. As the interlayer slippage is induced under shear deformations, the weakened shear resistance would lead to the reduced energy dissipation during sliding process. Our results provide valuable insight into fundamental mechanical properties of boron-doped graphene and its interfaces and potentially allows tailoring of interlayer coupling for low energy dissipation electromechanical devices.

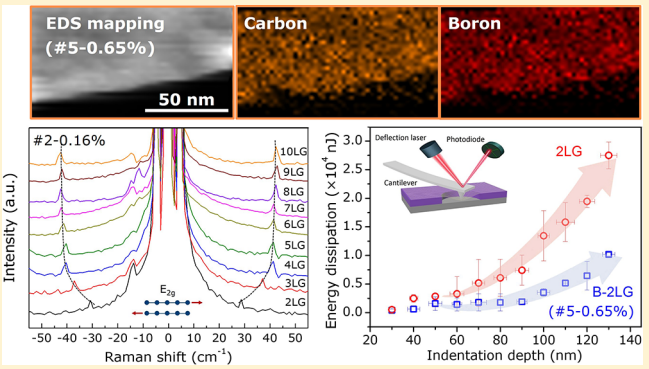

INTRODUCTION

Graphene, featuring intralayer covalent bonding and interlayer van der Waals coupling, exhibits unique in-plane properties (e.g., high carrier mobility, modulus and strength, thermal conductivity, and low optical absorbance) and exotic out-plane performances (e.g., nanoscale interlayer gallery for selective molecular permeation and nanolubrication).[1−5] To date, the interlayer coupling has been extensively investigated in terms of electrical and optical performance,[6−8] whereas a mechanical probing is complementary but currently lacking. Notably, the mechanical properties of multilayer graphene depend not only on its in-plane rigidity but also interlayer coupling particularly under shear mode. For instance, earlier works have demonstrated that the degradation in Young's modulus and the stiffening effect on bending stiffness took the principal responsibility from interlayer slippage of multilayer two-dimensional materials.[9−11] Nonetheless, despite substantial advances in theoretical modeling on the shear effects between neighboring graphene layers, the difficulty in experimental observations and measurements remains a vexing challenge. Such fact thus raises urgent needs in development of experimental strategies to understand the interlayer shear behavior in multilayer graphene systems and eventually to tune the interlayer coupling for high performance electronic as well as nanoelectromechanical (NEMS) devices.[2,12−15]

Chemical doping via incorporating heteroatoms into the crystal lattice tends to be an effective way to tailor interlayer coupling of multilayer graphene systems. Earlier works have revealed the subtle change in the interlayer spacing of boron-doped carbon materials (e.g., carbon fiber and HOPG), but the published data are always contradictory to each other.[16−20] Such discrepancy, on the one hand, lies possibly in different kinds of carbons investigated.[19] On the other hand, there exist several mechanisms for the change of interlayer spacing,

Received: June 13, 2017
Revised: November 5, 2017
Published: November 7, 2017

DOI: 10.1021/acs.jpcc.7b05771
J. Phys. Chem. C 2017, 121, 26034−26043

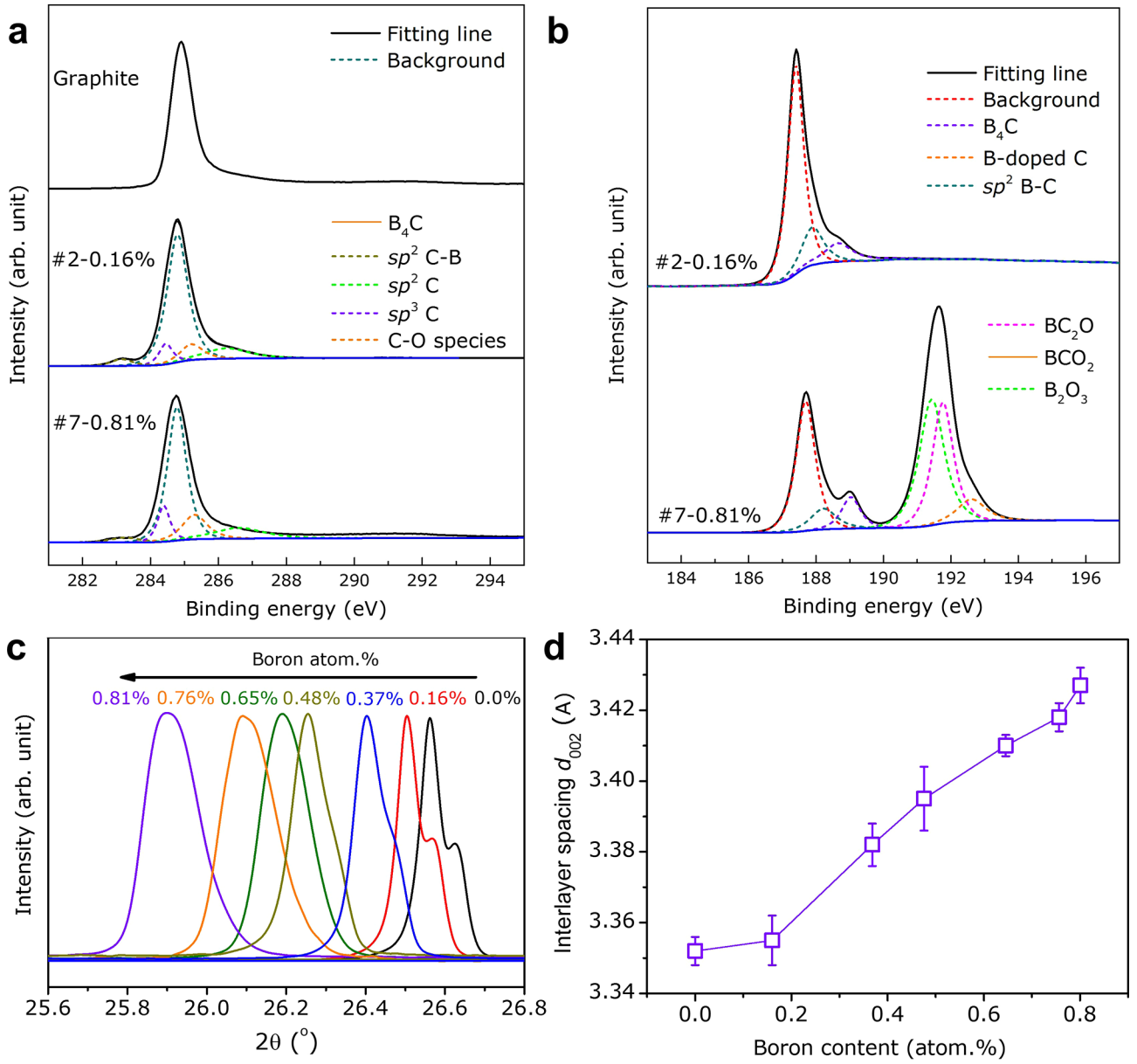

Figure 1. (a) C 1s XPS spectra of pristine graphite and boron-doped graphite with boron content of 0.16% and 0.81%, respectively. (b) The B 1s XPS spectra of boron-doped graphite with boron content of 0.16% and 0.81%, respectively. (c) X-ray diffraction pattern of graphite samples with different substitutional boron content. (d) The interlayer spacing of graphite as a function of the substitutional boron content.

including depleted π-electrons between graphitic layers, Poisson contraction effect and other factors involved, while their combined contributions remain unpredictable.[17,21] The common methods reported in previous works[16−20] to detect the interlayer structure information, such as X-ray diffraction (XRD) characterization, were mainly applicable to macro-size graphite. Recently, low-frequency Raman spectroscopy, which enables the interlayer deformation to be monitored in a nondestructive manner, affords a novel route toward revealing interlayer coupling in graphene at a microscopic level.[22−25] Consequently, monitoring chemically doped interfacial interactions in multilayer graphene is therefore essential both from a fundamental interest in understanding its atom-level interlayer interactions and from a technological perspective for its reliable applications.

In the present study, we report the first mechanical investigation into the effects of boron doping on the interlayer coupling behaviors of a multilayer graphene system. Boron-doped graphite with different boron contents was synthesized through high temperature thermal annealing treatment. Boron-doped graphene samples were prepared through micromechanical cleavage method, and the mechanical probing of their interlayer coupling was accomplished by micro-Raman shear modes detection. Our results indicate that the interlayer force constant of boron-doped graphene sheets exhibits a decreasing tendency with growing boron content, which is consistent with the increasing interlayer spacing from the XRD characterization of boron-doped graphite and further validated by molecular dynamics (MD) simulations. The decreased interlayer coupling would easily induce the interlayer slippage on bilayer graphene samples as indented by atomic force microscopy (AFM) probe, accompanied by the reduced energy dissipation. Our results will provide valuable insight into fundamental mechanical properties of boron-doped graphene

DOI: 10.1021/acs.jpcc.7b05771
J. Phys. Chem. C 2017, 121, 26034−26043

and its interfaces and shed further light on tailoring interlayer coupling in purpose for electromechanical applications.

EXPERIMENTAL METHODS

Sample Preparation and Characterization. Following well-developed strategies,[7] the boron doping process was achieved by mixing boron oxide with natural graphite and thermally treating the mixture at 2200 °C for about 2 h using a graphite furnace in an argon atmosphere. The weight ratio of boron oxide to graphite ranged from 0.5 to 50. The doping type and the boron content in the graphite were evaluated using X-ray photoelectron spectroscopy (XPS, ESCALAB 250Xi). The powder diffraction patterns of graphite before and after boron doping were obtained using synchrotron X-ray diffraction (XRD, Rigaku D/max-2500). The Raman spectra of graphite and exfoliated graphene on the SiO_2/Si substrate were measured with a Jobin-Yvon HR800 Raman system, equipped with a liquid-nitrogen-cooled charge-coupled detector. The laser excitation wavelengths are selected as 532 nm from a diode-pumped solid-state laser. HRTEM instruments (FEI Tecnai G2 F20 U-TWIN) were used for high-resolution imaging. STM experiments were carried out with a Nanoscope IIIa scanning probe microscope system (Veeco Metrology, U.S.A.) in ambient conditions.

Indentation Tests. Suspended graphene flakes were prepared on prepatterned silicon substrates covered with a 90 nm thick SiO_2 layer by micromechanical cleavage. An array of circular holes were fabricated by photolithography and reactive ion etching. The depth is ∼1 μm, and the diameter ranges from 0.5 to 1.5 μm. The nanoindentation test on the suspended graphene was performed using a commercial AFM system (Asylum Research, MFP-3D Infinity). Before each indentation, the samples were scanned in tapping mode to find graphene sheets fully covering a hole. After scanning, the AFM tip (NanoScience Instruments) was centered in the middle of the circular hole. Mechanical testing was performed using force−displacement mode. The force versus displacement curves obtained from the AFM nanoindentation tests were used to quantitatively determine the elastic stiffness of boron-doped graphene and the observed hysteresis loops enabled the estimation of the energy dissipation due to the possible slippage.

Molecular Dynamic (MD) Smulations. We used the LAMMPS package to perform all of the MD simulations.[26] Periodic boundary conditions were applied to a three-dimensional supercell of the boron-doped graphite, where the size of the supercell was 8.73 × 8.41 nm^2 and four layers of graphene were stacked in the Z direction. The Tersoff potential was used for the interatomic interaction between the carbon atoms and boron atoms in the same layer, which has been used to predict the structural, thermal, and mechanical properties of both carbon and boron nanostructure.[27,28] The interaction between carbon and boron atoms in the different layers were modeled using the Lennard-Jones 12-6 potential function with parameters ε_{C-C}, σ_{C-C}, ε_{C-B}, σ_{C-B}, ε_{B-B}, and σ_{B-B}. The Lorentz−Berthelot mixing rules were used to model the interactions between boron and carbon atoms in the different layers, that is, $\varepsilon_{C-B} = (\varepsilon_{C-C}\varepsilon_{B-B})^{1/2}$ and $\sigma_{C-B} = (\varepsilon_{C-C} + \varepsilon_{B-B})/2$, where ε_{C-C} = 0.004555 eV, σ_{C-C} = 0.3851 nm, ε_{B-B} = 0.00774 eV, and σ_{B-B} = 0.3630 nm are the parameters for interaction between carbon and boron atoms.[29] In our MD simulations, the atomic structure of graphite was equilibrated at T = 300 K by coupling to a Nosé−Hoover thermostat for 200 ps. The time step was 0.2 fs. The structure was further equilibrated in a microcanonical ensemble for 50 ps with the pressure of 1 bar in all three directions. Then the distance of interlayer graphene with B-doping was calculated from the MD simulations using the size of the simulation box.

RESULTS AND DISCUSSION

Structural Characterizations of Boron-Doped Graphene. We used natural graphite as a host material for boron doping via previously reported strategies (see the Experimental Methods section).[7] X-ray photoelectron spectroscopy (XPS) was utilized to verify the presence of the boron atoms and identify the boron content in graphite, ranging from ∼0.60% to ∼3.09% (Figure S1a). As shown in Figure 1a, the C 1s peak located at 284.8 eV is attributed to the sp^2 carbon atoms of the honeycomb lattice and there appears a slight downshift to 284.6 eV after boron doping, which corresponds to the lowering Fermi level through the formation of C−B bonds.[7] Besides, a new peak arose at 283.2 eV originates from the nonstoichiometric boron carbide (B_xC_y), especially B_4C, according to previous work.[30] Two distinct features at 284.4 and 285.3 eV are assigned to substitutional boron atoms into the honeycomb lattice and sp^3-carbon atoms, respectively. In addition, the component at 286.2 eV may correspond to the C−O species resulting from the contamination during thermal annealing.[30] The strong peak in the B 1s spectral region also corroborates the successful boron doping of the graphite as shown in Figure 1b, in which the components centered at 187.7 and 188.1 eV are attributed to B_4C and boron-doped carbon nanoparticles, respectively. The peak at 189.1 eV can be associated with the sp^2 C−B bonds present in graphene, indicative of the boron substitution.[31] The evolutions of the typical B 1s spectrum with increasing boron content are presented in Figure S1b, wherein the growth in the substitutional boron component is simultaneously observed. According to the curve fitted areas for B 1s spectra, the solubility of substitutional boron could hence be deduced, with the maximum of ∼0.81%, and the x-coordinate "boron content" in the following figures actually indicates the amount of substitutional boron atoms in graphene. At higher binding energy than 190 eV, three fitting peaks have been identified and denoted as different boron−oxygen−carbon compounds (C_2-BO at 191.4 eV and C-BO_2 at 191.8 eV) and boron oxide (B_2O_3 at 192.5 eV). Note that, as shown in Figure S1b, the oxygen species induced characteristic peak at ∼191 eV can be only visible in the samples with boron content higher than 0.76%, which possibly results from an overweight ratio of boron oxide to graphite and longer reaction time. Herein, we just intend to offer the comprehensive view of all of the elements included in the sample. As a matter of fact, the centroids of both C 1s and B 1s photoemission lines are slightly different from the reported results, wherein the discrepancy lies in distinct raw materials (e.g., natural graphite, graphene oxide, etc.), preparation methods (e.g., thermal annealing, chemical vapor deposition, electrothermal reactions, etc.), and consequently complex structures possessing oxy-boron-carbide species with different densities and distributions.[32−38]

Figure 1c displays the results of XRD of boron-doped graphite, where the (002) diffraction pattern has two distinct diffraction peaks initially. These two peaks arise from two different structures within the same graphite, including well-ordered structure and turbostratic structure.[39] With increasing boron content, the turbostratic fraction would be enhanced so

DOI: 10.1021/acs.jpcc.7b05771
J. Phys. Chem. C 2017, 121, 26034−26043

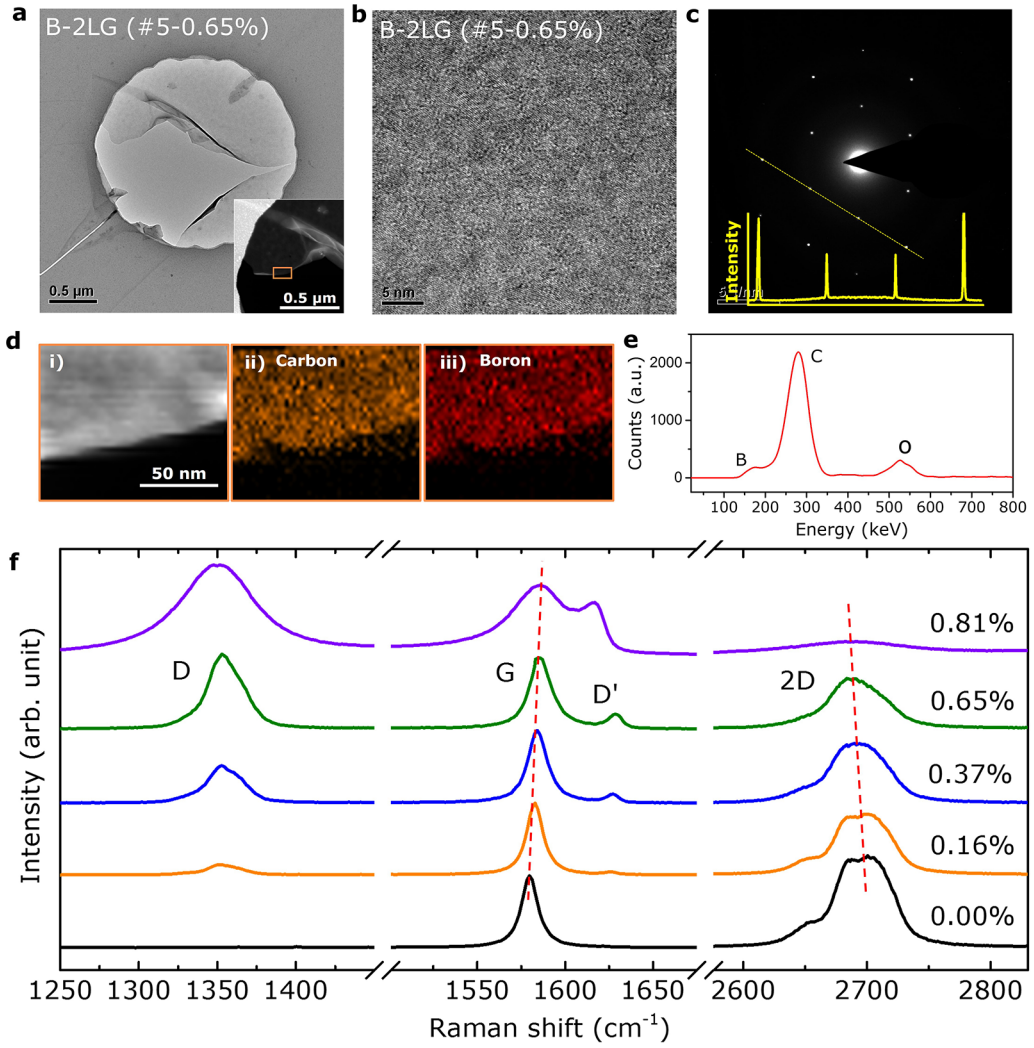

Figure 2. (a) TEM image of boron-doped bilayer graphene (B-2LG) with substitutional boron content of ~0.65%. The inset is the zoom-in HAADF image. (b) Atomic-scale TEM image of boron-doped bilayer graphene. (c) The SAED pattern and corresponding profile plot of diffraction peak intensities along the dashed line. (d-i) Dark field TEM image and EDS mapping of carbon (d-ii) and boron (d-iii) taken from the zoom-in region as marked by the rectangular in the inset of panel a. (e) The corresponding average EDS spectrum obtained from the boron-doped bilayer graphene in panel d-i. (f) Raman spectra of bilayer graphene with various boron content. The dashed lines are guided for eyes.

that the two peaks tend to merge into one peak with increasing full width at half-maximum (fwhm) up to 0.2°. Besides, the diffraction angle tends to decrease obviously as the boron content is improved (Figure S1c), corresponding to an increase in the interlayer spacing between graphene planes, as depicted in Figure 1d. This is in contrast to the previous results that the boron-doped graphite by substitution reaction shows a higher diffraction angle and shorter interlayer distance than that of pristine graphite.[7] As mentioned above, the variation of the interlayer spacing greatly depends on the competition between the weakened π-electron density and Poisson contraction effect, where the latter is responsible for the decrease in interlayer spacing.[17,21] In our case, however, boron doping gives rise to disordered structures due to the random existence of oxy-boron-carbide species, so that the weakened π-electron density between graphene planes possibly plays a more significant role than Poisson contraction to induce the enlarged interlayer spacing. Similar results have been reported in other works on carbon nanotubes (CNTs), where the average interlayer spacing of the boron-doped double-walled CNTs is enhanced to be 0.35−0.41 nm.[40,41] Additionally, Raman measurements were also performed to evidence the effective doping in graphite, where the stiffening of the Raman D-band and the degradation of the Raman 2D-band can be clearly observed in Figure S2.

Boron-doped graphene flakes were exfoliated by micromechanical cleavage of boron-doped graphite. Figure 2a,b shows the low- and high-resolution transmission electron microscopy (TEM) images of boron-doped bilayer graphene, displaying no distinctive differences in the texture compared with those of pristine ones (Figure S3a,b). The crystallinity is identified by the selected area electron diffraction (SAED) pattern in Figure 2c, where the 6-fold symmetry is clearly visible, suggesting the hexagonal lattice structure of graphene is maintained after boron doping. Based on the measurement of distances between reflex spots, the atomic separation in boron-doped graphene can be deduced as 1.59 Å. This value is relatively larger than the original bond length between carbon atoms (1.42 Å), which agrees well with the ever reported result extracted from scanning tunneling microscopy (STM).[42] Importantly, the line profile of the diffraction pattern shows the diffraction intensity ratio of the outer peaks over the inner

DOI: 10.1021/acs.jpcc.7b05771
J. Phys. Chem. C 2017, 121, 26034−26043

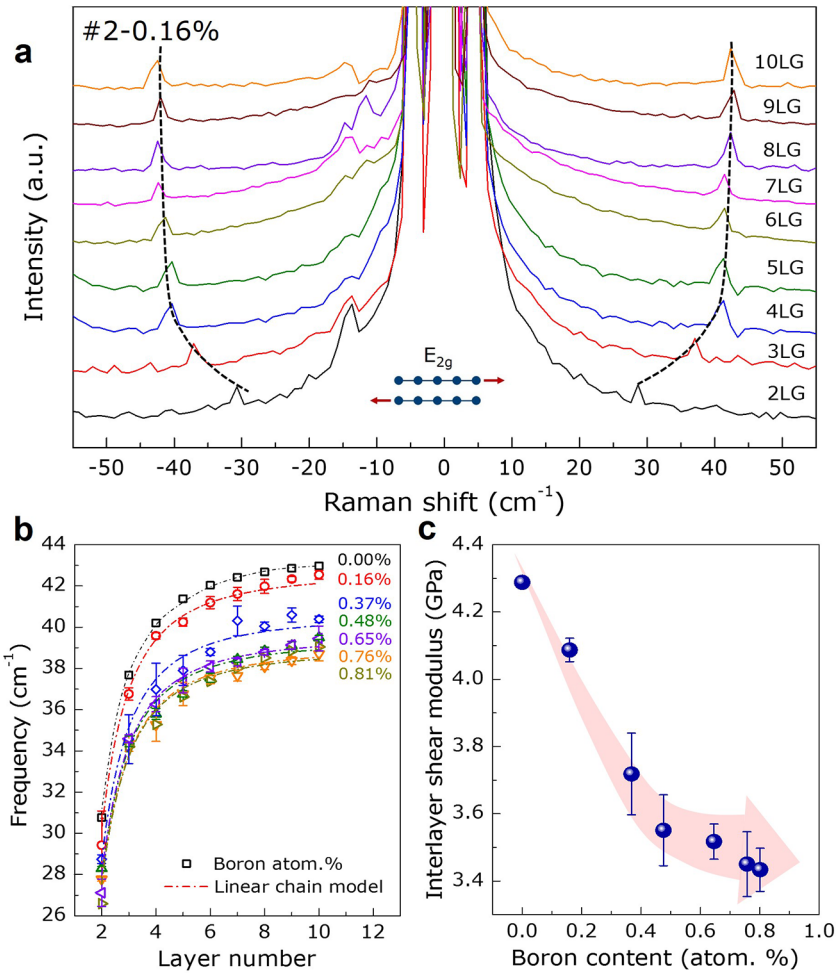

Figure 3. (a) Stokes and anti-Stokes Raman spectra for the C peak spectral region with increasing graphene layer numbers (substitutional boron content ~0.16%). The inset is the vibrational normal mode of interlayer shear (E_{2g}) mode in multilayer graphene. The dashed lines are guided for eyes. (b) Peak positions of C band as a function of layer numbers for samples with different boron content. The dash-dotted lines are the plots of eq 1 based on linear chain model. The black data points for pristine samples are from ref 22. (c) The calculated interlayer shear modulus as a function of boron content.

peaks close to 2.0, indicating the retained Bernal-stacked structure as well.[43,44] To further confirm the presence of boron element in boron-doped bilayer graphene, energy-dispersive spectroscopy (EDS) mapping was performed over the localized region in Figure 2d-i, as marked in the high angle annular dark field (HAADF) image (Figure 2a, inset). Carbon (Figure 2d-ii) and boron (Figure 2d-iii) signals were detected uniformly over the whole region, validating our structural design and indicating of a homogeneous boron doping in the graphene plane. In contrast with the carbon element, the seemingly analogous distribution of boron element is essentially attributed to strong background signals together with sparse boron atoms therein. As presented in the EDS spectrum (Figure 2e), the carbon peak is greatly stronger than the boron peak, which implies the considerably low boron content of doped graphene flakes. The electron energy loss spectroscopy (EELS) measurement was also performed to validate the substitutional boron atoms doped in graphene with retained hexagonal structure, as shown in Figure S4.

As a powerful nondestructive technique for identifying the doping of graphene,[45] Raman spectra further provide additional evidence of the introduction of boron atoms (Figure S5). Figure 2f plots the Raman spectrum of boron-doped bilayer graphene at different values of boron content. Compared with pristine graphene merely having G-band and 2D-band in general, two new featured peaks are visible, named D-band and D′-band, which are bound up with Raman double resonance process induced by the substitution of boron atoms as defect sites in graphene structure.[46] As a result, both the Raman D-band and D′-band are enhanced simultaneously with increasing boron content as depicted in Figure 2f. Remarkably, a plateau of I_D/I_G ratio can be observed at substitutional boron content >0.65% as shown in Figure S6a, implying the saturation of substitutional boron doping as well as the formation of structural voids.[7,47] This is consistent with the three-stage classification of disorder proposed by Ferrari and Robertson,[48] where the Raman intensity ratio I_D/I_G is proportional to the defect concentration at low defect density (stage 1) and inversely proportional at high defect density (stage 2). In addition, the full width at half-maximum (fwhm) of the G-band is also a measure to discriminate these two stages,[46] as it tends to be much bigger in stage 2 (Figure 2f). Figure S6b indicates in detail that the G-band fwhm is improved slightly at boron content <0.81%, due to the structural disorders induced by the incorporation of boron atoms in graphene lattice. As the boron content further increased to 0.81%, a substantial enhancement

DOI: 10.1021/acs.jpcc.7b05771
J. Phys. Chem. C 2017, 121, 26034−26043

up to 27 cm^{-1} is observed which corresponds to the formation of structural voids. Consequently, we can find that the samples in our experiment are most governed by stage 1. In fact, I_D/I_G can be utilized to calculate the defect density in graphene lattice, thus allowing us to estimate the boron content at the microscopic level based on the reported C−C and B−C bond lengths.[42,46] For a given $I_D/I_G = 2$, the boron content obtained from Raman results is approximated to be ∼0.03%, almost 1/20 of the value extracted from the XPS result (∼0.65%). Similar discrepancy between the XPS and Raman characterizations in the boron content can also be found in Kim's work.[7] One possible explanation is that the established model to determine the defect density is based on the Raman analysis for the point-like defects (e.g., monovacancy) in monolayer graphene subjected to ion bombardment.[46] For one thing, it might not be applicable for the bilayer graphene despite of the qualitative description of the relationship between I_D/I_G and boron density. For another, the distribution of boron atoms in graphene lattice might not be the same as the monovacancy. Some adjacent boron atoms might form an "island" so that calculated boron density is possibly related to the average distance between these "islands".[49]

Apart from the intensity and width, the Raman peak positions also exhibit slight variations with increasing boron content in graphene. In principle, boron doping as the hole doping, would alter the Femi energy of graphene and lead to the upshifts in both G- and 2D-bands.[50] Herein, slight G-band upshifts from ∼1580 to ∼1585 cm^{-1} are visible as expected, while the 2D-band is exceptionally downshifted from ∼2696 to ∼2688 cm^{-1} as shown in Figure 2f. Such a phenomenon was also demonstrated in Kim's work, and the underlying mechanism possibly lies in the softening caused by boron-induced tensile strains in graphene lattice.[7,51] The gradually decreased discrepancy between G- band 2D-bands frequencies also provides further validation, as shown in Figure S6c. Given the comparable Raman features (Figure S6) of boron-doped graphene exfoliated from the same graphite, herein, the doping level of graphene flakes is hence represented by the substitutional boron content of host graphite in the following discussions.

Interlayer Coupling of Boron-Doped Graphene. Earlier works have investigated the in-plane performances of boron-atom-incorporated graphene crystals,[52,53] while the impact on the interlayer coupling from a mechanical viewpoint has been unexplored yet. Recently, low-frequency Raman spectroscopy has been uncovered to be a diagnostic tool to explore the interlayer coupling.[22−25] For instance, in the case of graphite, there is merely one low-frequency E_{2g} mode denoted as C-band, which is responsible for the relative motion of atoms in two adjacent planes.[54] Tan el al. have revealed the Raman signature of the shear mode (C-band) of multilayer graphene and successfully measured the interlayer coupling strength as well as the interlayer shear modulus.[22] Furthermore, similar low-frequency Raman modes are observed in other layered materials, implying the universality of this technique can be expected for all 2D nanomaterials, such as MoS_2, WSe_2, black phosphorus, etc.[24,25,55] Thus, we employ Raman shear mode to provide a direct probe of interlayer interaction of boron-doped multilayer graphene. Figure 3a plots the low-frequency Raman spectra focusing on the C-peak spectral region for a set of boron-doped graphene samples with increasing layer numbers. Apparently, the boron doping enables peak profiles to be fitted well with Lorentz functions, rather than the Breit−Wagner−Fano line shape for pristine samples, suggesting the possible disappearance of the quantum interference between the C mode and a continuum of electronic transitions near the K point.[22] Herein, we use the notation NLG to indicate graphene with N layers (e.g., 1LG = monolayer). As the thickness decrease from 10LG to 2LG, the C-peak tends to downshift from ∼42 to ∼29 cm^{-1}, as guided by dashed lines. Such variation of peak positions can be interpreted by the linear chain model, essentially corresponding to the interlayer interactions of multilayer graphene.[22] Note that it has been demonstrated that the boron doping, classified as p-doping, typically results in upshift in Raman peaks as well.[56] However, herein, doping effect induced C-band shifts could be negligible as the consequent Raman shift is almost proportional to the corresponding peak positions. We can assert the reliability of utilizing Raman C-band shifts to elucidate the interlayer shear behaviors. Assuming that one layer interacts strongly only with adjacent layers and that the strength of this interlayer coupling is characterized by an interlayer force constant per unit area (α), the peak position of C-band for a given number layer is expressed by eq 1:[22]

$$\omega(\mathrm{C}) = \frac{1}{\sqrt{e}\pi c}\sqrt{\frac{\alpha}{\mu}}\sqrt{1+\cos\left(\frac{\pi}{N}\right)} \quad (1)$$

where c is the speed of light, $\mu = 7.6 \times 10^{-27}$ kg/Å^2 is the monolayer graphene mass per unit area, and N is the number of layers. By fitting the experimental data (dash-dotted line in Figure 3b), we are able to estimate the interlayer force constant and further deduce the interlayer shear modulus (G) from the perspective of elastic mechanics, by $G = \alpha t$ (t is the thickness of graphene). We then repeated detecting the Raman shear modes of boron-doped graphene samples with different boron contents and found a declined tendency of C-peak position with increasing doping level, as presented in Figure S7. In detail, a quantitative comparison of the experimental trends as well as the derived interlayer shear modulus for various boron contents is displayed in Figure 3b,c. As a result, the obtained interlayer force constant decreases from 12.8×10^{28} to 10.2×10^{28} N/m^3 with increasing boron content and such weakening of interlayer interactions would modify the electronic dispersion, leading to the resonant enhancement of C-band intensity (solid lines in Figure S7).[57] The interlayer shear modulus also drops by about 20% compared with the initial value at boron content lower than 0.65% and remains nearly constant with further increasing concentration. Such a two-stage feature can be actually interpreted by the structural evolution as manifested in the XPS spectrum (Figure S1b). It is envisioned that, at boron content from 0.16% to 0.65%, the substitutional boron plays the dominant role in the weakening of the interlayer coupling. As the boron content increases up to 0.76%, the saturation of substitutional boron solubility is nearly reached while additional surface species with increasing oxygen concentration have negligible influence on the interlayer coupling, so that a sluggish decreased tendency is expected as shown in Figure 3c. Besides that, the absolute values are consistent with results of previous works (e.g., ∼5.0 GPa in ref 58 and ∼4.6 GPa in ref 59),[58,59] implying the perfect Bernal-stacking of graphene flakes in our work. The reduced interlayer shear modulus is also in agreement with the enlarged interlayer spacing of graphite from the XRD results in Figure 1d. Undoubtedly, the modification of the interlayer coupling of graphene offers us a broader stage for multilayer graphene

DOI: 10.1021/acs.jpcc.7b05771
J. Phys. Chem. C 2017, 121, 26034−26043

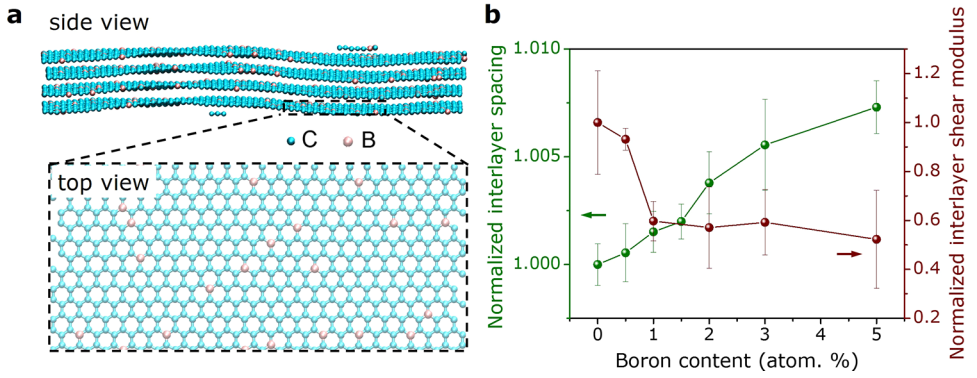

Figure 4. (a) Schematics of boron-doped multilayer graphene with side view and top view. (b) Normalized interlayer spacing and interlayer shear modulus as a function of the boron content.

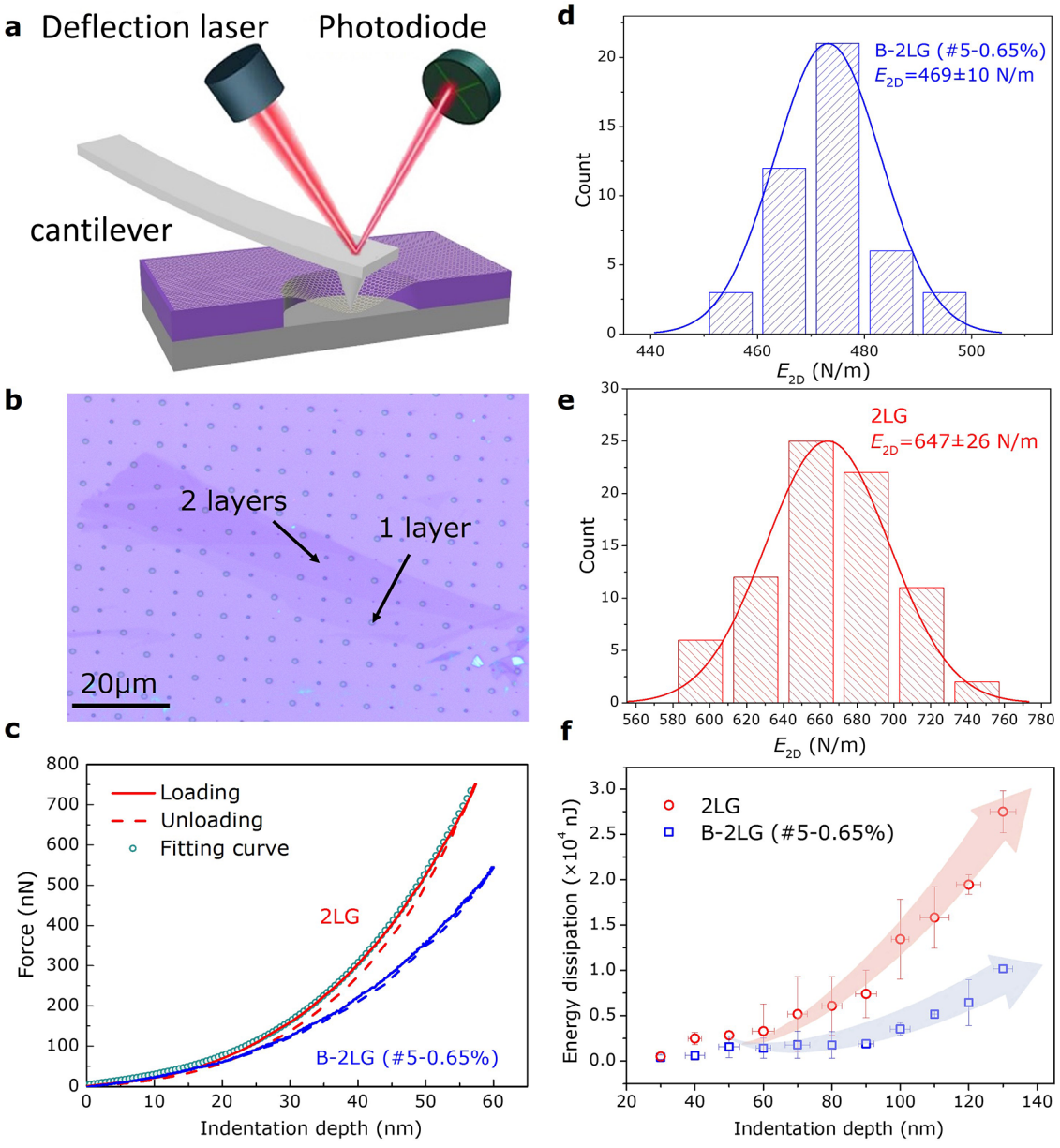

Figure 5. (a) Schematic of the experimental setup for nanoindentation. (b) Optical image of monolayer and bilayer graphene sheets covering the patterned holes on the silicon substrate. (c) Experimental loading/unloading curves for 2LG and B-2LG and corresponding histograms of Young's modulus for (d) B-2LG and (e) 2LG, respectively. (f) Energy dissipations as a function of indentation depth for 2LG and B-2LG, respectively.

DOI: 10.1021/acs.jpcc.7b05771
J. Phys. Chem. C 2017, 121, 26034−26043

based applications, such as resonators, sensors, and actuators, where interlayer shear has appreciable impacts on the mechanical deformation, vibration, and energy dissipation processes therein.[60]

A better insight into the underlying mechanism in the above-discussed experimental results can be obtained by performing MD simulations to clarify the interlayer behavior of multilayer graphene after boron doping. The schematics of the boron-doped multilayer graphene system are presented in Figure 4a, where boron atoms are randomly distributed in each layer. Expectedly, the substitutional boron atoms can weaken the π-electron density and hence the interactions between graphene layers, enlarging the interlayer spacing. Consequently, the interlayer spacing (d_{002}) exhibits an increasing tendency with the growing boron content as seen in Figure 4b. For instance, d_{002} for pristine graphene is 3.418 ± 0.006 Å while it is enhanced up to 3.438 ± 0.007 Å for graphene with boron content of ~3.0%. Note that, in our experiments, d_{002} increases from 3.352 ± 0.004 Å for pristine graphite to 3.427 ± 0.005 Å once reaching boron content of 3.0%. Such difference is definitely acceptable because, in simulations, boron atoms are entirely substitutional-type in graphene while it could not be guaranteed in experiments as some isolated atoms or clusters might be produced during thermally treating process, as evidenced in Figure 1a,b. However, it should be emphasized that it is the substitutional boron rather than the out-of-plane species that takes the main responsibility for the enlarged interlayer spacing. As shown in Figure S8, simulations are also performed for multilayer graphene with the introduction of 50% out-of-plane species and the enhancement in interlayer spacing could reach as high as 25%. Actually, such a substantial increase in the interlayer spacing caused by out-of-plane species has also been reported by previous works.[39,61] In contrast, the interlayer spacing measured in our experiment is only slightly improved (~2%) and much closer to the simulation result from graphene with all substitutional boron atoms. It hence claims the great contribution of substitutional boron to the interlayer spacing and hence interlayer coupling. In efforts to compare with Raman results, we also applied shear deformations into the system to directly reveal the interlayer shear modulus. In Figure 4b, the normalized interlayer shear modulus shows a decline for boron content <2.0% and then remains almost constant at higher doping level, agreeing with the experimental results. The only distinction is that simulation results present a relatively larger decrease (~50%) in interlayer shear modulus than that of experiments (~20%), which is probably resulted from the discrepancy of system dimensions as well as the evaluation methods. For one thing, tiny cell sizes in simulations might enable the influence of varied interlayer spacing to be magnified on the overall mechanical behavior. For another, additional factors should be taken into account in the shear loading, such as the surface roughness and loading rates, which are eschewed in Raman experiments.

Interlayer Sliding in Bilayer Graphene. Given the poor van der Waals binding in multilayer graphene, the mechanical performance of multilayer graphene sheets would be greatly affected by the interlayer slippage.[9,10,62−64] We thus perform nanoindentation tests (Figure 5a) with an AFM tip at the center of the suspended bilayer graphene membrane (Figure 5b), not only to characterize the interlayer slippage induced by the local shear deformation during indentation process but also to clarify the effect of the slippage on the energy dissipation during loading/unloading cycle.

The representative force−indentation curves for 2LG and boron-doped bilayer graphene (B-2LG) with substitutional boron content of ~0.65% are presented in Figure 5c and show a cubic dependence fitting the expression

$$F(\delta) = \pi\sigma_0\delta + \frac{E_{2D}}{a^2}\delta^3 \quad (2)$$

where F is the loading force, δ is the indentation at the central point, σ_0 is the pretension accumulated in the sheet during the preparation procedure, E_{2D} is the two-dimensional Young's modulus, and a is the radius. The results obtained from more than 30 drumheads yield histograms of E_{2D} as presented in Figure 5d,e, in which E_{2D} = 469 ± 10 N/m for B-2LG is lower than that of 2LG (E_{2D} = 647 ± 46 N/m). The decreased trend could be attributed to the imperfect structure of graphene caused by the introduction of boron atoms.[65,66] As expected, the increasing boron content would enhance the defect density and result in significant degradation in E_{2D}. Furthermore, an apparent hysteresis loop related to the interlayer energy dissipation during a loading/unloading cycle was observed in Figure 5c. Actually, indentation forces induced by the AFM tip tend to cause the local shear deformation and lead to interlayer slippage. With increasing indentation depth, the interlayer slippage tends to dissipate more energy as shown in Figure 5f. Compared to pristine 2LG, B-2LG exhibits a much lower energy dissipation as the unloading curve almost coincides with the loading curve. The decreased trend is ascribed to the relatively weaker interlayer coupling within a finite slippage distance. Moreover, the reduced energy dissipation by tuning the interlayer coupling seems to endow boron-doped graphene huge potential in multilayer graphene based nanoresonators as interlayer shear induced energy dissipation accounts for the critical loss mechanism on the Q-factors.[67] The less energy dissipation per vibrational cycle enabled the graphene NEMS to extend its operational lifetime by performing near optimal capacity for a longer period of time.[67]

To summarize, boron-doped graphene was prepared by mechanical cleavage and various doping levels were identified by XPS measurements. Through a joint study of the Raman shear modes, molecular dynamic simulations, and nano-indentations, we unveiled that the introduction of boron atoms could effectively modulate the interlayer coupling of multilayer graphene. The interlayer shear modulus is demonstrated to be reduced by ~20%, which coincides fairly well with the enlarged interlayer spacing. More interestingly, the interlayer slippage tends to be activated by the shear stress during the indentation process and identified by the closed hysteresis loop in the force−displacement curves. Accordingly, the attenuated interlayer coupling in boron-doped multilayer graphene could greatly weaken the shear interactions during the slippage and hence aid the interpretation for the suppressed energy dissipation. Our work hence highlights the significance of boron doping on tuning interlayer coupling as well as the mechanical performance of graphene and opens an avenue for other heteroatoms such as nitrogen, sulfur, silicon, and phosphorus, which require additional experimental and theoretical efforts. Moreover, controlled energy dissipation combined with enhanced electrochemical properties enable boron-doped graphene to hold enormous promise for applications in NEMS.

DOI: 10.1021/acs.jpcc.7b05771
J. Phys. Chem. C 2017, 121, 26034−26043

■ ASSOCIATED CONTENT

Supporting Information

The Supporting Information is available free of charge on the ACS Publications website at DOI: 10.1021/acs.jpcc.7b05771.

Characterization of boron-doped graphite and characterization of boron-doped graphene with different layer numbers. (PDF)

■ AUTHOR INFORMATION

Corresponding Authors

*E-mail: liulq@nanoctr.cn. Phone: +86 10 82545587. Fax: +86 10 62656765.

*E-mail: zhong.zhang@nanoctr.cn. Phone: +86-10-82545586. Fax: +86-10-82545586.

*E-mail: phtan@semi.ac.cn. Phone: +86-10-82304247. Fax: +86-10-82305056.

ORCID

Luqi Liu: 0000-0002-5752-1638

Zhiping Xu: 0000-0002-2833-1966

PingHeng Tan: 0000-0001-6575-1516

Notes

The authors declare no competing financial interest.

■ ACKNOWLEDGMENTS

This project was jointly supported by the National Key Basic Research Program of China (Grant Nos. 2013CB934203 and 2012CB937503, and 2016YFA0301200), the National Natural Science Foundation of China (Grant No. 21474023, 11434010, 11474277, and 11504077), the Youth Project of Hebei Province Natural Science Foundation (A2017201012), the Key Project of Hebei Province Department of Education Fund (ZD2017007), the Key Research Program of the Chinese Academy of Sciences (Grant No. XDPB06-02, XDPB08-2), and Beijing municipal science and technology commission.

■ REFERENCES

(1) Zhang, B.; Cui, T. H. An ultrasensitive and low-cost graphene sensor based on layer-by-layer nano self-assembly. *Appl. Phys. Lett.* **2011**, *98*, 073116.

(2) Bunch, J. S.; van der Zande, A. M.; Verbridge, S. S.; Frank, I. W.; Tanenbaum, D. M.; Parpia, J. M.; Craighead, H. G.; McEuen, P. L. Electromechanical resonators from graphene sheets. *Science* **2007**, *315*, 490−493.

(3) Shahil, K. M. F.; Balandin, A. A. Graphene-multilayer graphene nanocomposites as highly efficient thermal interface materials. *Nano Lett.* **2012**, *12*, 861−867.

(4) Nair, R. R.; Wu, H. A.; Jayaram, P. N.; Grigorieva, I. V.; Geim, A. K. Unimpeded permeation of water through helium-leak-tight graphene-based membranes. *Science* **2012**, *335*, 442−444.

(5) Liu, Z.; Yang, J.; Grey, F.; Liu, J. Z.; Liu, Y.; Wang, Y.; Yang, Y.; Cheng, Y.; Zheng, Q. Observation of microscale superlubricity in graphite. *Phys. Rev. Lett.* **2012**, *108*, 205503.

(6) Wu, J. B.; Hu, Z. X.; Zhang, X.; Han, W. P.; Lu, Y.; Shi, W.; Qiao, X. F.; Ijias, M.; Milana, S.; Ji, W.; et al. Interface coupling in twisted multilayer graphene by resonant Raman spectroscopy of layer breathing modes. *ACS Nano* **2015**, *9*, 7440−7449.

(7) Kim, Y. A.; Fujisawa, K.; Muramatsu, H.; Hayashi, T.; Endo, M.; Fujimori, T.; Kaneko, K.; Terrones, M.; Behrends, J.; Eckmann, A.; et al. Raman spectroscopy of boron-doped single-layer graphene. *ACS Nano* **2012**, *6*, 6293−6300.

(8) Wu, J.; Rodrigues, M. T.; Vajtai, R.; Ajayan, P. M. Tuning the electrochemical reactivity of boron- and nitrogen-substituted graphene. *Adv. Mater.* **2016**, *28*, 6239−6246.

(9) Wei, X.; Meng, Z.; Ruiz, L.; Xia, W.; Lee, C.; Kysar, J. W.; Hone, J. C.; Keten, S.; Espinosa, H. D. Recoverable slippage mechanism in multilayer graphene leads to repeatable energy dissipation. *ACS Nano* **2016**, *10*, 1820−1828.

(10) Liu, K.; Yan, Q.; Chen, M.; Fan, W.; Sun, Y.; Suh, J.; Fu, D.; Lee, S.; Zhou, J.; Tongay, S.; et al. Elastic properties of chemical-vapor-deposited monolayer MoS_2, WS_2, and their bilayer heterostructures. *Nano Lett.* **2014**, *14*, 5097−5103.

(11) Chen, X.; Yi, C.; Ke, C. Bending stiffness and interlayer shear modulus of few-layer graphene. *Appl. Phys. Lett.* **2015**, *106*, 101907.

(12) Soldano, C.; Mahmood, A.; Dujardin, E. Production, properties and potential of graphene. *Carbon* **2010**, *48*, 2127−2150.

(13) Allen, M. J.; Tung, V. C.; Kaner, R. B. Honeycomb carbon: A review of graphene. *Chem. Rev.* **2010**, *110*, 132−145.

(14) Liu, X.; Suk, J. W.; Boddeti, N. G.; Cantley, L.; Wang, L.; Gray, J. M.; Hall, H. J.; Bright, V. M.; Rogers, C. T.; Dunn, M. L.; et al. Large arrays and properties of 3-terminal graphene nanoelectromechanical switches. *Adv. Mater.* **2014**, *26*, 1571−1576.

(15) Schwierz, F. Graphene transistors. *Nat. Nanotechnol.* **2010**, *5*, 487−496.

(16) Endo, M.; Kim, C.; Karaki, T.; Nishimura, Y.; Matthews, M. J.; Brown, S. D. M.; Dresselhaus, M. S. Anode performance of a Li ion battery based on graphitized and B-doped milled mesophase pitch-based carbon fibers. *Carbon* **1999**, *37*, 561−568.

(17) Wu, X.; Radovic, L. R. Inhibition of catalytic oxidation of carbon/carbon composites by boron-doping. *Carbon* **2005**, *43*, 1768−1777.

(18) Hach, C. T.; Jones, L. E.; Crossland, C.; Thrower, P. A. An investigation of vapor deposited boron rich carbon - a novel graphite-like material - part I: the structure of BC_x (C_6B) thin films. *Carbon* **1999**, *37*, 221−230.

(19) Kim, E.; Oh, I.; Kwak, J. Atomic structure of highly ordered pyrolytic graphite doped with boron. *Electrochem. Commun.* **2001**, *3*, 608−612.

(20) Naeini, J. G.; Way, B. M.; Dahn, J. R.; Irwin, J. C. Raman scattering from boron-substituted carbon films. *Phys. Rev. B: Condens. Matter Mater. Phys.* **1996**, *54*, 144−151.

(21) Hishiyama, Y.; Inagaki, M. Lattice parameter changes in graphite with boron doping. *Carbon* **2001**, *39*, 150−152.

(22) Tan, P. H.; Han, W. P.; Zhao, W. J.; Wu, Z. H.; Chang, K.; Wang, H.; Wang, Y. F.; Bonini, N.; Marzari, N.; Pugno, N.; et al. The shear mode of multilayer graphene. *Nat. Mater.* **2012**, *11*, 294−300.

(23) Wang, H.; Feng, M.; Zhang, X.; Tan, P. H.; Wang, Y. In-phase family and self-similarity of interlayer vibrational frequencies in van der Waals layered materials. *J. Phys. Chem. C* **2015**, *119*, 6906−6911.

(24) Zhao, Y.; Luo, X.; Li, H.; Zhang, J.; Araujo, P. T.; Gan, C. K.; Wu, J.; Zhang, H.; Quek, S. Y.; Dresselhaus, M. S.; et al. Interlayer breathing and shear modes in few-trilayer MoS_2 and WSe_2. *Nano Lett.* **2013**, *13*, 1007−1015.

(25) Cong, C.; Yu, T. Enhanced ultra-low-frequency interlayer shear modes in folded graphene layers. *Nat. Commun.* **2014**, *5*, 4709−4715.

(26) Plimpton, S. Fast parallel algorithms for short-range molecular-dynamics. *J. Comput. Phys.* **1995**, *117*, 1−19.

(27) Lindsay, L.; Broido, D. Optimized Tersoff and Brenner empirical potential parameters for lattice dynamics and phonon thermal transport in carbon nanotubes and graphene. *Phys. Rev. B: Condens. Matter Mater. Phys.* **2010**, *81*, 205441.

(28) Kınacı, A.; Haskins, J. B.; Sevik, C.; Çağın, T. Thermal conductivity of BN-C nanostructures. *Phys. Rev. B: Condens. Matter Mater. Phys.* **2012**, *86*, 115410.

(29) Wang, Y.; Xu, Z. Water intercalation for seamless, electrically insulating, and thermally transparent interfaces. *ACS Appl. Mater. Interfaces* **2016**, *8*, 1970−1976.

(30) Shirasaki, T.; Derre, A.; Menetrier, M.; Tressaud, A.; Flandrois, S. Synthesis and characterization of boron-substituted carbons. *Carbon* **2000**, *38*, 1461−1467.

(31) Cattelan, M.; Agnoli, S.; Favaro, M.; Garoli, D.; Romanato, F.; Meneghetti, M.; Barinov, A.; Dudin, P.; Granozzi, G. Microscopic view

on a chemical vapor deposition route to boron-doped graphene nanostructures. *Chem. Mater.* **2013**, *25*, 1490−1495.
(32) Sheng, Z. H.; Gao, H. L.; Bao, W. J.; Wang, F. B.; Xia, X. H. Synthesis of boron doped graphene for oxygen reduction reaction in fuel cells. *J. Mater. Chem.* **2012**, *22*, 390−395.
(33) Tang, Y. B.; Yin, L. C.; Yang, Y.; Bo, X. H.; Cao, Y. L.; Wang, H. E.; Zhang, W. J.; Bello, I.; Lee, S. T.; Cheng, H. M.; et al. Tunable band gaps and p-type transport properties of boron-doped graphenes by controllable ion doping using reactive microwave plasma. *ACS Nano* **2012**, *6*, 1970−1978.
(34) Wang, L.; Sofer, Z.; Šimek, P.; Tomandl, I.; Pumera, M. Boron-doped graphene: scalable and tunable p-type carrier concentration doping. *J. Phys. Chem. C* **2013**, *117*, 23251−23257.
(35) Yen, W. C.; Medina, H.; Huang, J. S.; Lai, C. C.; Shih, Y. C.; Lin, S. M.; Li, J. G.; Wang, Z. M.; Chueh, Y. L. Direct synthesis of graphene with tunable work function on insulators via in situ boron doping by nickel-assisted growth. *J. Phys. Chem. C* **2014**, *118*, 25089−25096.
(36) Peng, Z.; Ye, R.; Mann, J. A.; Zakhidov, D.; Li, Y.; Smalley, P. R.; Lin, J.; Tour, J. M. Flexible boron-doped laser-induced graphene microsupercapacitors. *ACS Nano* **2015**, *9*, 5868−5875.
(37) Usachov, D. Y.; Fedorov, A. V.; Petukhov, A. E.; Vilkov, O. Y.; Rybkin, A. G.; Otrokov, M. M.; Arnau, A.; Chulkov, E. V.; Yashina, L. V.; Farjam, M.; et al. Epitaxial B-graphene: large-scale growth and atomic structure. *ACS Nano* **2015**, *9*, 7314−7322.
(38) Agnoli, S.; Favaro, M. Doping graphene with boron: a review of synthesis methods, physicochemical characterization, and emerging applications. *J. Mater. Chem. A* **2016**, *4*, 5002−5025.
(39) Jones, L. E.; Thrower, P. A. Influence of boron on carbon fiber microstructure, physical properties and oxidation behavior. *Carbon* **1991**, *29*, 251−269.
(40) Panchakarla, L. S.; Govindaraj, A.; Rao, C. N. R. Nitrogen-and boron-doped double-walled carbon nanotubes. *ACS Nano* **2007**, *1*, 494−500.
(41) Lyu, S. C.; Han, J. H.; Shin, K. W.; Sok, J. H. Synthesis of boron-doped double-walled carbon nanotubes by the catalytic decomposition of tetrahydrofuran and triisopropyl borate. *Carbon* **2011**, *49*, 1532−1541.
(42) Endo, M.; Hayashi, T.; Hong, S. H.; Enoki, T.; Dresselhaus, M. S. Scanning tunneling microscope study of boron-doped highly oriented pyrolytic graphite. *J. Appl. Phys.* **2001**, *90*, 5670−5674.
(43) Ta, H. Q.; Perello, D. J.; Duong, D. L.; Han, G. H.; Gorantla, S.; Nguyen, V. L.; Bachmatiuk, A.; Rotkin, S. V.; Lee, Y. H.; Rummeli, M. H. Stranski-Krastanov and Volmer-Weber CVD growth regimes to control the stacking order in bilayer graphene. *Nano Lett.* **2016**, *16*, 6403−6410.
(44) Lee, S.; Lee, K.; Zhong, Z. Wafer scale homogeneous bilayer graphene films by chemical vapor deposition. *Nano Lett.* **2010**, *10*, 4702−4707.
(45) Zhan, D.; Sun, L.; Ni, Z. H.; Liu, L.; Fan, X. F.; Wang, Y. Y.; Yu, T.; Lam, Y. M.; Huang, W.; Shen, Z. X. $FeCl_3$-based few-layer graphene intercalation compounds: single linear dispersion electronic band structure and strong charge transfer doping. *Adv. Funct. Mater.* **2010**, *20*, 3504−3509.
(46) Cancado, L. G.; Jorio, A.; Ferreira, E. H.; Stavale, F.; Achete, C. A.; Capaz, R. B.; Moutinho, M. V.; Lombardo, A.; Kulmala, T. S.; Ferrari, A. C. Quantifying defects in graphene via Raman spectroscopy at different excitation energies. *Nano Lett.* **2011**, *11*, 3190−3196.
(47) Zandiatashbar, A.; Lee, G. H.; An, S. J.; Lee, S.; Mathew, N.; Terrones, M.; Hayashi, T.; Picu, C. R.; Hone, J.; Koratkar, N. Effect of defects on the intrinsic strength and stiffness of graphene. *Nat. Commun.* **2014**, *5*, 3186−3194.
(48) Ferrari, A. C.; Robertson, J. Interpretation of Raman spectra of disordered and amorphous carbon. *Phys. Rev. B: Condens. Matter Mater. Phys.* **2000**, *61*, 14095−14107.
(49) Gajurel, P.; Kim, M.; Wang, Q.; Dai, W.; Liu, H.; Cen, C. Vacancy-Controlled Contact Friction in Graphene. *Adv. Funct. Mater.* **2017**, *27*, 1702832−1702839.
(50) Das, A.; Pisana, S.; Chakraborty, B.; Piscanec, S.; Saha, S. K.; Waghmare, U. V.; Novoselov, K. S.; Krishnamurthy, H. R.; Geim, A. K.; Ferrari, A. C.; et al. Monitoring dopants by Raman scattering in an electrochemically top-gated graphene transistor. *Nat. Nanotechnol.* **2008**, *3*, 210−215.
(51) Mohiuddin, T. M. G.; Lombardo, A.; Nair, R. R.; Bonetti, A.; Savini, G.; Jalil, R.; Bonini, N.; Basko, D. M.; Galiotis, C.; Marzari, N.; et al. Uniaxial strain in graphene by Raman spectroscopy: G peak splitting, Grüneisen parameters, and sample orientation. *Phys. Rev. B: Condens. Matter Mater. Phys.* **2009**, *79*, 205433.
(52) Kawai, S.; Saito, S.; Osumi, S.; Yamaguchi, S.; Foster, A. S.; Spijker, P.; Meyer, E. Atomically controlled substitutional boron-doping of graphene nanoribbons. *Nat. Commun.* **2015**, *6*, 8098−8103.
(53) Usachov, D. Y.; Fedorov, A. V.; Vilkov, O. Y.; Petukhov, A. E.; Rybkin, A. G.; Ernst, A.; Otrokov, M. M.; Chulkov, E. V.; Ogorodnikov, I. I.; Kuznetsov, M. V.; et al. Large-scale sublattice asymmetry in pure and boron-doped graphene. *Nano Lett.* **2016**, *16*, 4535−4543.
(54) Nemanich, R. J.; Lucovsky, G.; Solin, S. Infrared active optical vibrations of graphite. *Solid State Commun.* **1977**, *23*, 117−120.
(55) Ling, X.; Liang, L.; Huang, S.; Puretzky, A. A.; Geohegan, D. B.; Sumpter, B. G.; Kong, J.; Meunier, V.; Dresselhaus, M. S. Low-frequency interlayer breathing modes in few-layer black phosphorus. *Nano Lett.* **2015**, *15*, 4080−4088.
(56) Zhao, W.; Tan, P. H.; Liu, J.; Ferrari, A. C. Intercalation of few-layer graphite flakes with $FeCl_3$: Raman determination of Fermi level, layer by layer decoupling, and stability. *J. Am. Chem. Soc.* **2011**, *133*, 5941−5946.
(57) Wu, J. B.; Zhang, X.; Ijas, M.; Han, W. P.; Qiao, X. F.; Li, X. L.; Jiang, D. S.; Ferrari, A. C.; Tan, P. H. Resonant Raman spectroscopy of twisted multilayer graphene. *Nat. Commun.* **2014**, *5*, 5309−5316.
(58) Bosak, A.; Krisch, M.; Mohr, M.; Maultzsch, J.; Thomsen, C. Elasticity of single-crystalline graphite: Inelastic x-ray scattering study. *Phys. Rev. B: Condens. Matter Mater. Phys.* **2007**, *75*, 153408.
(59) Shen, Y. K.; Wu, H. A. Interlayer shear effect on multilayer graphene subjected to bending. *Appl. Phys. Lett.* **2012**, *100*, 101909.
(60) Liu, Y.; Xu, Z.; Zheng, Q. The interlayer shear effect on graphene multilayer resonators. *J. Mech. Phys. Solids* **2011**, *59*, 1613−1622.
(61) Hou, J.; Shao, Y.; Ellis, M. W.; Moore, R. B.; Yi, B. Graphene-based electrochemical energy conversion and storage: fuel cells, supercapacitors and lithium ion batteries. *Phys. Chem. Chem. Phys.* **2011**, *13*, 15384−15402.
(62) Han, J.; Ryu, S.; Kim, D.-K.; Woo, W.; Sohn, D. Effect of interlayer sliding on the estimation of elastic modulus of multilayer graphene in nanoindentation simulation. *EPL Europhys. Lett.* **2016**, *114*, 68001.
(63) Lee, C.; Wei, X.; Li, Q.; Carpick, R.; Kysar, J. W.; Hone, J. Elastic and frictional properties of graphene. *Phys. Status Solidi B* **2009**, *246*, 2562−2567.
(64) Xu, L.; Ma, T. B.; Hu, Y. Z.; Wang, H. Molecular dynamics simulation of the interlayer sliding behavior in few-layer graphene. *Carbon* **2012**, *50*, 1025−1032.
(65) Neek-Amal, M.; Peeters, F. M. Nanoindentation of a circular sheet of bilayer graphene. *Phys. Rev. B: Condens. Matter Mater. Phys.* **2010**, *81*, 68001.
(66) Koenig, S. P.; Boddeti, N. G.; Dunn, M. L.; Bunch, J. S. Ultrastrong adhesion of graphene membranes. *Nat. Nanotechnol.* **2011**, *6*, 543−546.
(67) Kim, S. Y.; Park, H. S. Multilayer friction and attachment effects on energy dissipation in graphene nanoresonators. *Appl. Phys. Lett.* **2009**, *94*, 101918.

DOI: 10.1021/acs.jpcc.7b05771
J. Phys. Chem. C 2017, 121, 26034−26043